DTU Library

Reversible Decomposition of Secondary Phases in BaO Infiltrated LSM Electrodes-Polarization Effects

Traulsen, Marie Lund; McIntyre, Melissa D.; Norrman, Kion; Sanna, Simone; Mogensen, Mogens Bjerg; Walker, Robert A.

Link back to DTU Orbit

Full Paper

Reversible Decomposition of Secondary Phases in BaO Infiltrated LSM Electrodes –

Polarization Effects

Marie L. Traulsen*, Melissa D. McIntyre, Kion Norrman, Simone Sanna, Mogens B. Mogensen and Robert A. Walker

Dr. M. L. Traulsen, Dr. K. Norrman, Dr. S. Sanna, Prof. M. B. Mogensen
Department of Energy Conversion and Storage, Technical University of Denmark
Frederiksborgvej 399, 4000 Roskilde, Denmark
E-mail: matr@dtu.dk

M. D. McIntyre, Prof. R. A. Walker
Department of Chemistry and Biochemistry, Montana State University
Bozeman, MT 59717-1734, Montana, USA

In operando Raman spectroscopy is used to study ceramic $La_{0.85}Sr_{0.15}MnO_{3\pm\delta}$ (LSM)

electrodes infiltrated with BaO. The aim of this work is to clarify why BaO infiltration

reduces the polarization resistance in oxygen containing atmospheres. Prior to the *in operando*

experiments, *ex situ* XRD and Raman spectroscopy reveals the formation of a secondary

phase, $Ba_3Mn_2O_8$, on the electrode. During the *in operando* Raman investigation of the BaO

infiltrated $La_{0.85}Sr_{0.15}MnO_{3\pm\delta}$ electrodes, experiments are performed at 300 °C and 500 °C

with oxygen partial pressure 0.1 atm and with -1V or +1V applied potential. A changing

electrode surface is observed during operation as the $Ba_3Mn_2O_8$ secondary phase decomposes

and manganese oxide accumulates on the electrode surface during cathodic polarization. The

observed changes are reversible. These results suggest that the formation of $Ba_3Mn_2O_8$ is

responsible for the reduced polarization resistance observed at OCV in an oxygen containing

atmosphere. Furthermore, the results illustrate the dramatic differences between the electrode

1

surface composition at OCV and during cathodic polarization. Overall, the results highlight the dynamic interactions between minor secondary phases and applied potential, a general effect that may be important for the high performance frequently observed with ceramic electrodes prepared by infiltration.

1. Introduction

Understanding the surface chemistry of ceramic electrodes is important for a diverse range of electrocatalytic technologies including fuel cells[1], electrolysis cells[2] and electrochemical gas purification systems.[3] A popular approach for improving the electrocatalytic properties of ceramic electrodes employs infiltration during electrode manufacturing.[4, 5] During the infiltration step, a material is added in the form of an aqueous precursor solution to an existing scaffold, where the desired material forms during subsequent conditioning of the electrode.[5] An unintended consequence of this approach can be the formation of minor secondary phases, either from the infiltrate itself[6], or from reactions between the infiltrate and the scaffold.[7] Recent investigations on $La_{1-x}Sr_xCoO_{3-\delta}$ (LSC) based electrodes have indicated that the presence of minor secondary phases may even improve electrode performance[6, 8-10] due to the formation of hetero-interfaces.[8-10] These and other studies of secondary phases often draw conclusions correlating electrode composition with performance based on *ex situ* studies and *in operando* electrochemical characterization. The *ex situ* analyses performed before and after usage provide valuable insight into irreversible changes that occur in electrode composition and structure while *in operando* electrochemical measurements report on how performance changes with different operating conditions. Both approaches – *ex situ* studies and *in operando* electrochemical characterization – fail to produce direct molecular and materials specific information about the chemical condition of the electrode *in operando*. Electrochemical characterization and materials specific data acquired *in operando* are

2

necessary to understand and improve electrocatalytic properties such as activity, selectivity and durability. Here we define *in situ* studies as studies in which one or two parameters such as temperature, electrical polarization, or atmosphere reflect operating conditions while in *in operando* studies all three parameters correspond to realistic values during operation of ceramic electrodes. The importance of such measurements was demonstrated recently by Backhaus-Ricoult et al.[11] and Siebert et al.[12] who employed *in situ* XPS and *in operando* Raman spectroscopy, respectively, in studies of perovskite based electrodes and their electrocatalytic properties. Data showed reversible changes in composition[11] and structure[12] of perovskite oxide electrodes during electrical polarization that could only be observed with *in operando* spectroscopic measurements. When the electrode returned to open circuit voltage (OCV), the electrode composition resumed its pre-operational state.

One of the most thoroughly investigated perovskites used for ceramic electrodes has been strontium doped lanthanum manganite (LSM), primarily due to the material's high electronic conductivity at high temperatures and the good compatibility with the commonly used yttria stabilized zirconia (YSZ) electrolyte.[13] In order to improve the performance of LSM based electrodes for SOFC applications, especially at lower temperatures, experiments with infiltrated LSM electrodes have been conducted including infiltration of the entire LSM phase[14-16], infiltration with noble metals or single oxides as "dopants" [17-19] and infiltration with high performance oxygen ion conductors.[5] Similarly, LSM based electrodes for electrochemical gas purification have been infiltrated to improve their electrocatalytic properties towards conversion of gaseous pollutants.[20-23] Infiltration with BaO, possibly with $BaCO_3$ as the final product has been observed to cause a significant reduction in the polarization resistance on LSM-based electrodes.[21, 24, 25] The effect of the BaO infiltration has been attributed to changes in processes related to adsorption, dissociation and charge transfer for the gaseous reactant; however, exactly how BaO infiltration affects these

processes has not yet been clarified[21, 24, 25], and as pointed out by Hong et al.[24] attention

should be paid to the chemical bonding state of the Ba atom in the surface of the electrodes.

In order to identify the reason(s) for improved performance observed with BaO modified

LSM electrodes in an oxygen atmosphere[21, 24, 25] and to identify the behavior of secondary

phases under operating conditions, the studies described in this work employed *in operando*

Raman spectroscopy coupled with electrochemical measurements. Thin film LSM model

electrodes with and without BaO modification were employed, and the studies were

conducted under realistic operating conditions for intermediate temperature SOFCs and

electrochemical gas conversion cells. Changes in electrode composition were examined as a

function of temperature and electrical polarization. The data suggest that at OCV conditions

$Ba_3Mn_2O_8$, a secondary phase formed during the infiltration step, is responsible for the

reduced polarization resistance. Furthermore the data showed significant, reversible changes

in the electrode surface composition with an applied electrical polarization on the electrodes,

resulting in a change in the MnO_x species at the electrode surface and reversible

decomposition of a secondary phase, $Ba_3Mn_2O_8$, with cathodic polarization.

2. Results

LSM thin film electrodes were characterized by TOF-SIMS and XPS before and after the *in*

operando Raman spectroscopy. Results from the pre- and post-characterization are described

below together with the *in operando* Raman spectroscopy results. Furthermore, evidence of

the secondary $Ba_3Mn_2O_8$ phase in a conventional, porous LSM-CGO electrode is reported.

2.1 Pre-characterization of LSM thin films

The LSM electrodes used in these studies had the nominal composition $(La_{0.85}Sr_{0.15})_{0.9}MnO_{3\pm\delta}$,

where the LSM perovskite structure had a slight deficiency on the A-site. Four of these LSM

thin films without BaO were characterized by means of TOF-SIMS and XPS. A

representative TOF-SIMS depth profile for one of the thin films is shown in Figure 1, after the

signal intensity for the individual elements has been corrected for the total signal intensity to

minimize instrumental effects. The TOF-SIMS profile (Figure 1) shows an approximately 25

nm thick surface layer of the LSM with a composition deviating from the bulk LSM

composition (TOF-SIMS measurements have a depth resolution of ≈2 nm for these materials).

Within this surface layer, Mn appears to be depleted and La enriched compared to the bulk

values for LSM. Variation in the concentration profiles of individual elements is also

observed throughout the layer (Figure 1b). Compared to bulk LSM, Sr appears to be enriched

within the 5 nm layer next to the gas-solid interface and depleted at depths from 5 nm to 25

nm. The Mn concentration within the first 5 nm next to the gas-solid interface shows a slight

increase towards the interface but never exceeds the bulk value. Furthermore, the LaO

concentration profile reaches a maximum at 7 nm's depth. Overall these distributions indicate

the existence of two surface layers: a top layer dominated by Sr and Mn and an inner layer

enriched in La. These findings agree with reports from similarly prepared electrodes.[26] We

note that care must be taken when interpreting TOF-SIMS profiles on LSM electrodes, as

matrix-effect may cause artifacts to appear in the concentration profile.[26] For this reason the

four LSM electrodes were analyzed by XPS to yield quantitative information on the electrode

composition within a probe depth of 5-10 nm. The results from the XPS analysis of four LSM

films are reported in Table 1, where the measured ratios between the elements are compared

to the theoretical ratios. The XPS results are in agreement with the results from the TOF-

SIMS depth profile and show enrichment in A-site cations (La, Sr) relative to the B-site cation

(Mn), with the Sr enrichment being more pronounced than the La enrichment. Sr segregation

on the surface of perovskites has been observed previously and is believed to influence the

electrode performance, but the specific influence of Sr's enrichment at the electrode surface is

still debated.[27, 28] In conclusion, both XPS and TOF-SIMS show Sr enrichment at the LSM

thin film surface, and the TOF-SIMS furthermore reveals that within a 25 nm surface layer of

the LSM electrode the composition deviates from the bulk LSM composition.

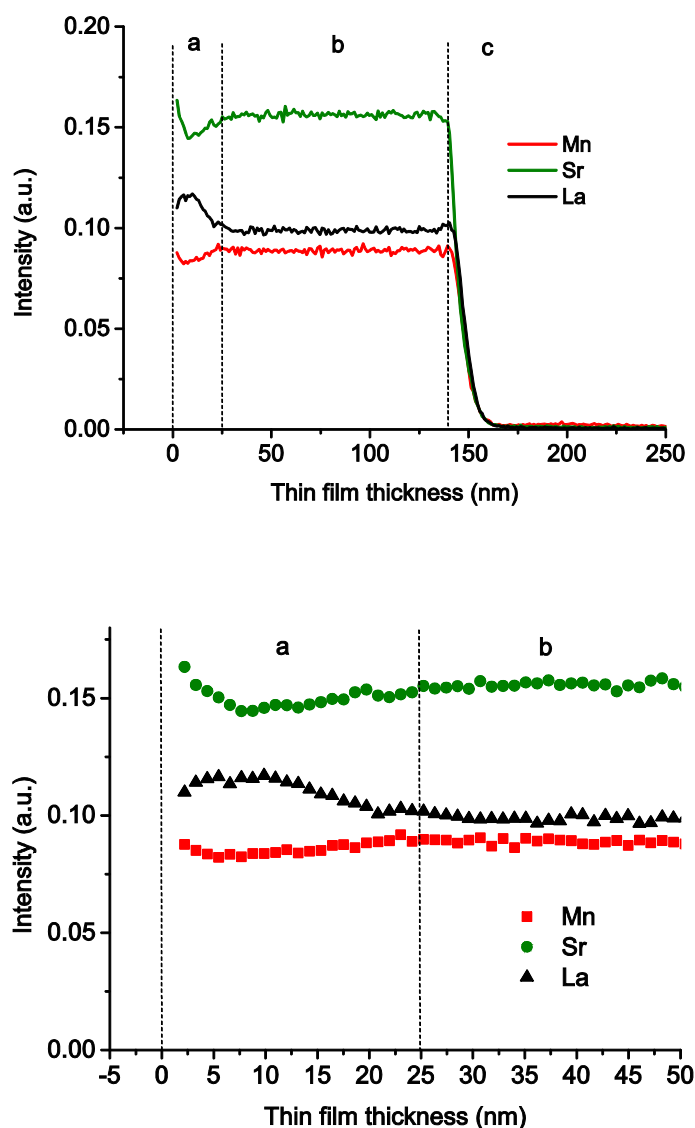**Figure 1.** TOF-SIMS depth profile through un-tested LSM thin film, the entire thin film is

shown in the top and the 50 nm closest to the gas-solid interface is shown in the bottom. The

letters state the following a) 25 nm thick LSM surface layer with composition different from

the bulk electrode, b) bulk LSM electrode and c) CGO thin film below the LSM electrode.

The intensity is proportional to the concentration of the elements.

Table 1. Ratio between metallic electrode elements in $(La_{0.85}Sr_{0.15})_{0.9}MnO_{3\pm\delta}$ as synthesized and measured at the surface of 4 un-tested LSM thin films by XPS, probing depth 5-10 nm.

	As synthesized ratio	Measured ratio	Measured/As synthesized
Sr/La	0.176	0.27 ±0.04	1.53
Sr/Mn	0.135	0.41 ±0.07	3.04
La/Mn	0.765	1.49 ±0.15	1.95
(La+Sr)/Mn	0.9	1.91 ±0.17	2.12

2.2 Post-mortem characterization of LSM thin film with BaO

The LSM thin film electrode with BaO was characterized by ToF-SIMS after the *in operando* Raman spectroscopy experiments. The depth profiles for the electrode elements show less well-defined electrode interfaces (Figure 2) compared to the untested LSM-thin electrodes. This difference is ascribed to the sample preparation rather than being a result from the *in operando* experiments. The depth profile for the Ba shows diffusion of Ba from the surface through the entire LSM electrode.
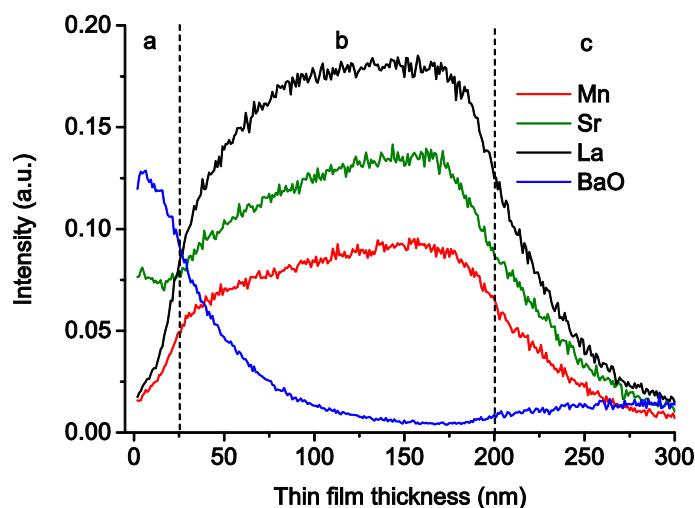
Figure 2. Post mortem ToF-SIMS depth profile through LSM thin film electrode impregnated with BaO. The letters state a) the surface layer, b) the bulk LSM electrode and c) the CGO thin film below the LSM electrode. The Ba depth profile shows diffusion of Ba into the LSM electrode.

2.3 Presence of $Ba_3Mn_2O_8$ on BaO-infiltrated LSM electrodes

XRD data collected on BaO infiltrated porous LSM-CGO electrodes revealed a minor peak at 24.1° likely due to $BaCO_3$ (ICSD 91888) and three minor peaks in the diffraction pattern at 2θ locations of 27.7°, 31.4° and 42.2 ° (SI-1). These latter features correspond to the three dominant peaks of $Ba_3Mn_2O_8$ (ICSD 280045), one of the few compounds in which Mn is present in an oxidation state of +5. This material presumably formed during electrode processing since it was not present during the initial stages of fabrication. As $Ba_3Mn_2O_8$ is not commercially available, $Ba_3Mn_2O_8$ was synthesized according to the procedure described by Weller et al.,[29] and characterized by XRD and Raman spectroscopy, the latter revealing two characteristic peaks at ≈301 cm^{-1} and 771 cm^{-1}. Details concerning $Ba_3Mn_2O_8$ synthesis are reported in SI-2 together with XRD and Raman data from the pure compound.

2.4 Raman spectroscopy

In the following sections, results from the Raman experiments are presented, including spectra recorded on thin model electrodes with and without BaO deposition. However at first a comparison between the porous LSM-CGO electrode and the thin film electrode is made.

2.4.1 Reproducibility between porous LSM-CGO electrode and LSM thin film model electrode

Raman spectra recorded from a porous LSM-CGO electrode (SI-3) were consistent with the results from the thin film electrode with respect to the presence of $Ba_3Mn_2O_8$. In contrast to the thin film electrode, presence of MnO_x and $BaCO_3$ was not detected in the porous LSM-CGO though $BaCO_3$ residues from the impregnation were detected on the edge of the porous electrode, as evidenced by stronger more well-defined 690 cm^{-1} and 1050 cm^{-1} peaks, and and likely gave rise to the aforementioned weak $BaCO_3$ signal in the XRD. The presence of MnO_x and $BaCO_3$ on the pristine thin film electrode and not in the porous electrode is assigned to differences in the preparation method, and does not influence the conclusions drawn on $Ba_3Mn_2O_8$ in this paper. .

2.4.2 Similarities and differences between pure LSM electrodes and electrodes with BaO deposition

Representative *in situ* Raman spectra collected from thin film LSM electrodes without and with BaO deposition exposed to 0.1 atm O_2 in Ar at 500 °C are shown in Figure 3. Spectra recorded prior to polarization show clearly the compositional differences between electrodes. The most distinct vibrational feature for the pure LSM thin film electrode is a broad peak at 610 cm^{-1}. Vibrational modes of both YSZ[30, 31] and MnO_x [32, 33] species are found in this region. For cells with thin film electrodes, this feature may therefore arise from MnO_x on the electrode surface/within the electrode and/or from the YSZ substrate below the electrode. Cells with the screen printed LSM-CGO electrode (SI-4) did not contain YSZ but showed a

similar peak around 610 cm^{-1} that can result only from MnO$_x$ species. The literature reports some discrepancy on peak assignments for the vibrational Raman modes of MnO$_x$ species.[32, 33] Some of this uncertainty can be attributed to material changes induced by exposure to high intensity fields including laser light.[32, 34] Furthermore, the different phases of MnO$_x$ all have vibrational features between 570-690 cm^{-1}. Given these considerations and a preponderance of evidence in the literature, the 610 cm^{-1} peak is assigned tentatively to MnO$_2$.[32], [35, 36] This assignment is also consistent with XPS results by Backhaus-Ricoult et al. that showed Mn in an oxidation state of +4 on the unpolarised LSM surface.[11]

In contrast to the pure LSM thin film electrode, the BaO modified LSM thin film electrode exhibits several sharper bands in the Raman spectrum. Two features are observed consistently at 306 cm^{-1} and 773 cm^{-1} on the electrodes with BaO. The 306 cm^{-1} and 773 cm^{-1} peaks are assigned to a Ba$_3$Mn$_2$O$_8$ secondary phase and are discussed in more detail below. In addition to these features, a peak at 1051 cm^{-1} was observed and the intensity of this peak varied strongly with the position on the sample. Since MnO has peak at 1050 cm^{-1} [37] and BaCO$_3$ a peak at 1052 cm^{-1} [38] the observed peak is tentatively assigned to one of these two species.
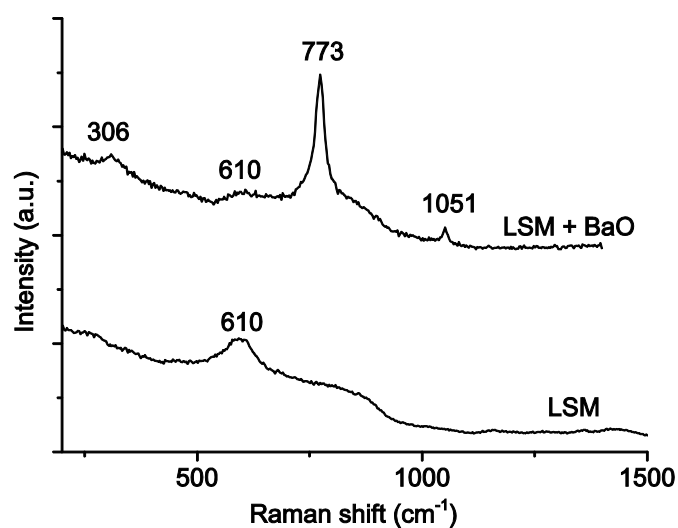
Figure 3. Representative Raman spectra recorded on a LSM thin film electrode with and without BaO infiltration at 500 °C in 10% oxygen flow. The top spectrum is displaced vertically to facilitate comparison.

Table 2 summarizes assignments for materials observed in the Raman spectra during the experiments on the thin films samples. All peaks were not present simultaneously, but depended on the sample and experimental conditions.

Table 2 Overview of all peaks observed in the Raman spectra recorded on the thin film samples; note all peaks may not be observed simultaneously

Raman shift [cm^{-1}]	Assignment	Reference
306	$Ba_3Mn_2O_8$	This work, see SI-2
610	YSZ	[30, 31]
610 (broad and weak)	MnO_x, most likely MnO_2	[33, 35, 39]
644	MnO_x, most likely Mn_3O_4	[32, 33]

662	MnO_x, most likely Mn_2O_3	[33]
690	$BaCO_3$	[38, 40]
771	$Ba_3Mn_2O_8$	This work , see SI-2
1050	MnO	[37]
1052	$BaCO_3$	[38]

2.4.3 Effect of applied potential on electrode surface composition

In operando Raman measurements were performed to investigate how electrode composition

changed as a function of applied potential and temperature. Experimental parameters are

summarized in Table 3. With two exceptions, measurement series were conducted at least

twice for each combination of parameters to confirm the reproducibility of the results. In

general, the chronoamperometry curves recorded during cathodic polarizations showed a

small deactivation during the first ≈600 s, resulting in a 10-20% decrease in the current

density, (see SI-4). After these initial changes, the current density stayed stable indicating the

electrode did not suffer further degradation during the experiments.

Table 3. The parameters used during the *in operando* Raman characterization

Parameter	Values
Atmosphere	0.1 atm O_2 in Ar
Temperature	300 °C, 500 °C
Applied voltage	OCV, -1 V, +1 V

The following section describes how the chemical species detected with Raman spectroscopy

were influenced by operational conditions. Raman spectra recorded at 500 °C prior to, during

and after cathodic polarization of -1 V are shown in Figure 4a) and Figure 4b) together with

the corresponding changes in selected peak intensities plotted in Figure 4c). Finally, Figure 5

shows a peak intensity plot for a similar experiment conducted at 500 °C; however, in this

case the cell polarization was switched to +1 V immediately after the -1 V polarization.

Electrodes exhibited consistent qualitative behaviors with respect to polarization at 300 °C

and 500 °C. Spectra from the electrode operating at 300 °C are reported in SI-5.

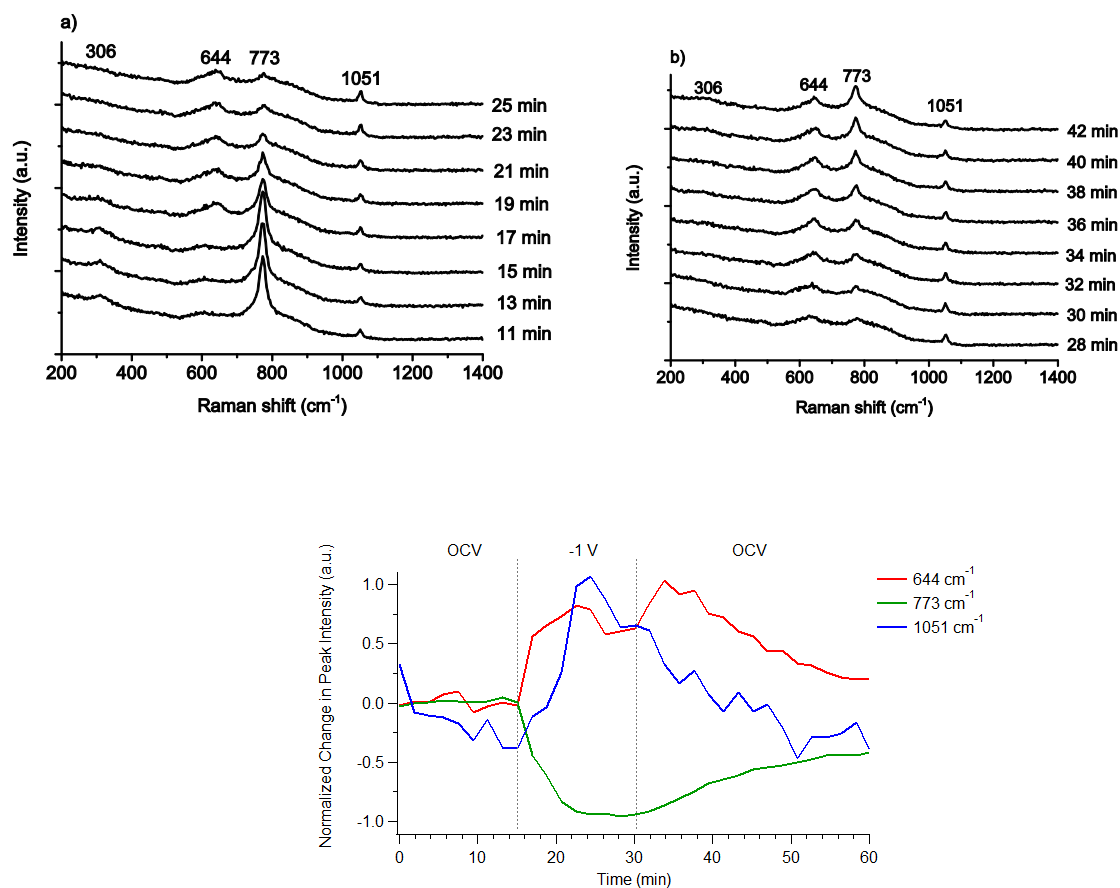**Figure 4.** Raman spectra on BaO infiltrated LSM thin film electrode at 500 °C with 10% O_2: a) before and during the onset of -1 V b) at -1 V followed by OCV and c) the normalized peak intensity plot for the data set shown in a) and b).
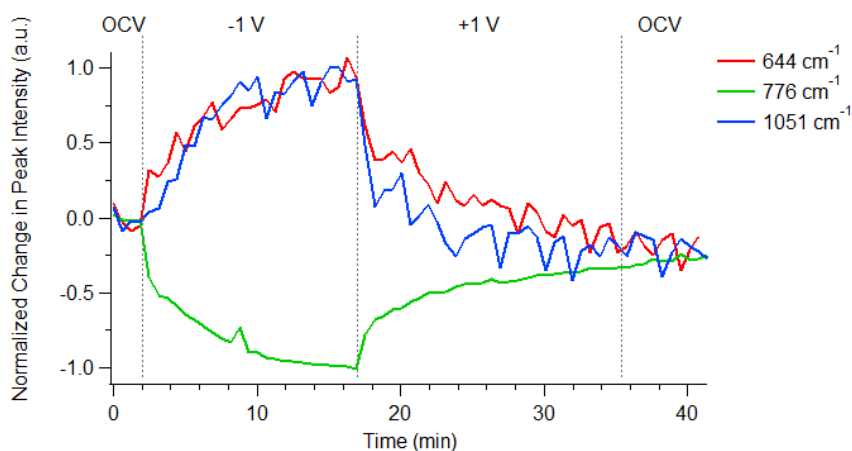

Figure 5. Peak intensity plot from Raman spectra on BaO infiltrated LSM thin film electrode at 500 °C with 10% O_2 during -1 V polarization followed immediately by +1 V polarization.

$Ba_3Mn_2O_8$: The formation and decomposition of $Ba_3Mn_2O_8$ was characterized by reversible increases or decreases, respectively, of the 306 cm^{-1} and 773 cm^{-1} peak intensities. Raman spectra showed that in a 0.1 atm O_2 environment, the $Ba_3Mn_2O_8$ vibrational band intensity diminished during cathodic polarization at -1 V (Figure 4 and Figure 5) and increased to an asymptotic limit during anodic polarization at +1 V (Figure 5). Similarly, when the cell was held at OCV after cathodic polarization, the $Ba_3Mn_2O_8$ peak intensities increased (Figure 4c), but at a slower rate compared to the increase observed during anodic polarization. Taken together, these observations show that the amount of the $Ba_3Mn_2O_8$ secondary phase in an infiltrated electrode depends strongly on the applied potential, in this case ranging from almost full decomposition at cathodic polarization to full regeneration at OCV or anodic polarization.

MnO_x: In addition to the MnO_2 peak at 610 cm^{-1}, a broad vibrational band was observed at approximately 644 cm^{-1}. Contrary to the behavior observed for the 773 cm^{-1} feature assigned to $Ba_3Mn_2O_8$, the signal at 644 cm^{-1} *increased* upon cathodic polarization of the electrode (Figure 4 and Figure 5). This feature is most likely a signature of Mn_3O_4 given literature reports of a dominant band at 650 cm^{-1} in spectra collected at room temperature.[32, 33] Furthermore, these prior studies have also shown that MnO_2 and Mn_2O_3 may be converted into Mn_3O_4 due to localized heating from the laser excitation source used for the Raman measurements.[32-34, 41] In Figure 4c and Figure 5 the formation of Mn_3O_4 is anticorrelated with the loss of $Ba_3Mn_2O_8$. These results suggest that $Ba_3Mn_2O_8$ decomposition is a dominant source for the observed Mn_3O_4 formation. The Mn_3O_4 expulsion from the LSM electrode itself during cathodic polarization cannot be excluded either, since the peak intensity plots occasionally show an increase in the Mn_3O_4 occurring faster than the decrease in the $Ba_3Mn_2O_8$ signal (see SI-6). We propose that under reducing conditions, the $Ba_3Mn_2O_8$ (where Mn is in a +5 oxidation state) decomposes into Mn_3O_4 (with mixed Mn^{2+}/Mn^{3+} character). The resulting Ba-containing material eluded detection in these experiments, and in

this connection it is noted the absence of CO_2 in the gas flow make generation of $BaCO_3$ unlikely. A change in the 1051 cm^{-1} peak was observed upon polarization as the peak increased during cathodic polarization and decreased during subsequent OCV and anodic polarization (Figure 4 and Figure 5). However, this increase in intensity was only observable when the 1051 cm^{-1} was either small or non-existant prior to the polarization. If a large, dominant peak at 1051 cm^{-1} was present in spectra before the polarization, no effect of cathodic polarization was observed, yet a decrease was still observed during anodic polarization (see SI-5). This result is explained by the coincidence between the $BaCO_3$ peak at 1052 cm^{-1} and the MnO peak at 1050 cm^{-1}, as the strong $BaCO_3$ peak occasionally overshadowed changes in the weak MnO peak. The $BaCO_3$ was not affected during cathodic polarization, but partly oxidized during anodic polarization. The MnO was formed during cathodic polarization and removed during anodic polarization. The correlation between the polarization induced changes in the MnO_x species and the $Ba_3Mn_2O_8$ will be discussed further on the "Discussion" section.

The transformations observed with cathodic polarizations were reversible. Once the cathodic polarization was removed, the vibrational signature for $Ba_3Mn_2O_8$ began to reappear (Figure 4b and Figure 4c), eventually approaching its original intensity prior to the -1V polarization. Changing the bias immediately from -1V to +1V accelerated the regeneration of $Ba_3Mn_2O_8$ (Figure 5). Interestingly, when the cathodic polarization (-1V) was changed to OCV, the $Ba_3Mn_2O_8$ began to grow back immediately, albeit slowly, while the Mn_3O_4 signal continued to increase for several minutes before eventually returning to pre-cathodic polarization levels (Figure 4c). The continued growth of the Mn_3O_4 signal after the cathodic polarization was removed is ascribed to re-oxidation of MnO and is discussed below.

Finally, we note that all of the spectroscopic measurements show that material changes happen on the order of minutes or tens of minutes when the cell is polarized at 300 °C or 500 °C, with the most dramatic material changes occurring within the first 5 minutes. Thus,

WILEY-VCH

ex situ techniques or *in situ* measurements without sufficient temporal resolution will not be able to resolve compositional changes occurring in these high temperature materials during operation.

3. Discussion

3.1 Electrode surface composition at OCV conditions

BaO infiltration of LSM electrodes has in previous work, based on electrochemical impedance spectroscopy at OCV conditions, been reported to cause a significant decrease in the polarization resistance.[21, 24, 25] The aim in the present study is to investigate the reason for this decrease, which, depending on reaction conditions and sample preparation, may be as large as an order of magnitude.[21, 24, 25] Raman spectroscopy performed with electrodes at OCV revealed the presence of $Ba_3Mn_2O_8$ on the BaO infiltrated LSM electrodes to be the only consistent difference between infiltrated and non-filtrated electrodes. For this reason $Ba_3Mn_2O_8$ is suggested to cause the reduced polarization resistance at OCV observed when LSM electrodes are infiltrated with BaO. Unfortunately there are to the best of the author's knowledge no reports in literature on the electrical properties of $Ba_3Mn_2O_8$. However, work described by Roos et al.[42] may provide insight into the electrical properties of $Ba_3Mn_2O_8$ since Roos et al. explain manganese ions in tetrahedral coordination as in $Ba_3Mn_2O_8$ can easily change from Mn^{5+} to Mn^{4+} and from Mn^{4+} to Mn^{3+}, which may contribute to the observed enhancement of the electrode's electrocatalytic properties. The suggestion that $Ba_3Mn_2O_8$ causes the reduced polarization resistance at OCV is made with the reservation that for each reporting in the literature, both the amount of Ba infiltrate and the LSM stoichiometry play a role in secondary phase formation and the possible formation of $BaCO_3$, which may also influence the electrocatalytic properties[24]. However, regardless of the impregnation method and materials choice, electrodes in a real application are subjected to

17

electrical polarization, for which reason the effect of cathodic and anodic polarization on the

BaO infiltrated LSM electrode was investigated in this study.

3.2 Electrical polarization and electrode surface composition

The *in operando* Raman spectra presented in Figure 4 and Figure 5 demonstrate clearly that

the surfaces of a BaO-infiltrated LSM-electrode are dynamic and significantly affected by an

applied polarization. The discussion below focuses on how the dominant species on the

electrode surface, $Ba_3Mn_2O_8$ and MnO_x, are affected by the applied reaction conditions.

3.2.1 $Ba_3Mn_2O_8$: Under 0.1 atm O_2 in Ar, $Ba_3Mn_2O_8$ showed a strong dependence on the

applied electrical polarization where cathodic polarization promoted decomposition and

anodic polarization promoted the regeneration of $Ba_3Mn_2O_8$ on the LSM electrode. Cathodic

polarization has the same effect on LSM electrodes as very low oxygen partial pressures, a

condition that promotes the formation of oxygen vacancies.[43] Continued exposure to high

cathodic polarization conditions and/or low the oxygen partial pressure ultimately leads to

decomposition of LSM electrodes[44-46] and will also decompose complex oxides like

$Ba_3Mn_2O_8$. The Ba-Mn-O diagram[47] (Figure 6) shows that the total oxide content in the

$Ba_3Mn_2O_8$ only needs to decrease 4% for the material to transform into a different

stoichiometric compound. Furthermore, the diagram reveals that if the oxide content is

reduced by 4-5% a region is reached in which several Ba-Mn-O and Mn-O compounds can

coexist, which corresponds well with the increase in different MnO_x species observed on the

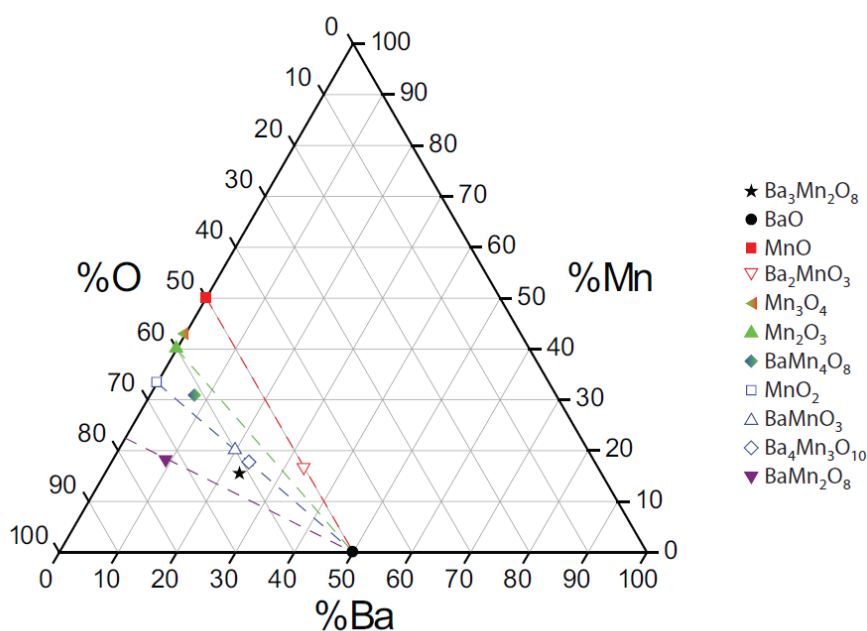electrode surface during cathodic polarization in this study.

Figure 6. Ba-Mn-O ternary diagram showing $Ba_3Mn_2O_8$ (black star) and other phases. Compounds with the Mn Valence of +2 (red) +3 (green) , +4(blue) and +7 (purple) are grouped by color and connected by dashed lines, while compounds with mixed Mn valence have a gradient between the colors representing the two different valences. The diagram is re-printed from the dissertation thesis of Eric C. Samulon[47].

3.2.2 MnOx: The *in operando* Raman spectra show that the amount of Mn_3O_4 on the electrode surface increased significantly during cathodic polarization and decreased during anodic polarization. We propose that the dominant source of the Mn_3O_4 is $Ba_3Mn_2O_8$ given that during the majority of the polarizations the intensity of the $Ba_3Mn_2O_8$ and the Mn_3O_4 Raman signal appear directly anti-correlated. Expulsion of Mn_3O_4 from the LSM electrode itself during cathodic polarization may also be a minor source for Mn_3O_4, as expulsion of Mn_3O_4 from LSM previously has been observed *ex situ* by XRD on LSM samples sintered at low oxygen partial pressure ($pO_2=10^{-6}$ atm).[46] Furthermore expulsion of MnO/Mn_3O_4 has been reported on LSM and lanthanum manganite electrodes during cyclic voltammetry.[45] *Ex situ*

ToF-SIMS studies of LSM microelectrodes have also revealed a strong, *irreversible* redistribution of the Mn from the electrode onto the electrolyte after electrical polarization.[26] *In situ* studies of manganese redistribution on LSM electrodes are scarce. Among the few literature reports is work by Backhaus-Ricoult et al., who detected polarization induced reduction and migration of Mn-species onto the electrolyte by XPS under conditions approximating those employed in solid oxide fuel cell systems.[11] Results from the *in operando* Raman measurements generally agree with findings from the aforementioned studies in terms of the capability of a cathodic polarization to re-distribute Mn in/on the LSM electrode. However, the Raman data imply Mn_3O_4 enrichment during cathodic polarization whereas the *in situ* XPS study showed Mn depletion at the electrode surface during cathodic polarization.[11] The discrepancy is likely explained by a combination of: (1) the presence of $Ba_3Mn_2O_8$ that acts as a Mn_3O_4 source in this work, (2) Backhaus-Ricoult using stoichiometric $La_{0.8}Sr_{0.2}MnO_3$[11] while the present study employed A-site deficient $(La_{0.85}Sr_{0.15})_{0.9}MnO_{3\pm\delta}$, and/or (3) diffusion of Ba-ions into the LSM, as evident from the ToF-SIMS characterization (Figure 2) altering cation segregation mechanism(s).

One interesting observation of Mn_3O_4 observed *in operando* considers the behavior of Mn_3O_4 at OCV following cathodic polarization. After the Raman signal from Mn_3O_4 increases and stabilizes during cathodic polarization, the Mn_3O_4 increases even further during the first 3-5 min at OCV *after* the polarization has been removed at 500 °C (Figure 4). These observations appear contradictory, namely that applying a cathodic polarization causes an increase in the Mn_3O_4 signal, and the removal of the cathodic polarization is accompanied by a Mn_3O_4 signal intensity that increases even further. A plausible explanation of this phenomenon hinges on the labile nature of Mn^{n+}. In $Ba_3Mn_2O_8$, Mn has a formal oxidation state of 5+. Under cathodic polarization of -1 V, Raman spectra show that reduced forms of Mn (i.e. Mn^{3+} and Mn^{2+}) become more prevalent, given the growth of vibrational signatures at 644 cm^{-1} (Mn_3O_4)

and 1050 cm^{-1} (MnO). When the bias is removed or reversed, thermodynamic considerations will once again favor more oxidized forms of Mn, leading eventually to the fully recovered amount of Mn^{5+} in Ba$_3$Mn$_2$O$_8$. Given the availability of mobile oxide ions, we propose that as MnO begins to oxidize, Mn$_3$O$_4$ forms as an intermediate species on a path that ultimately results in Ba$_3$Mn$_2$O$_8$ and accounts for the growth in the 644 cm^{-1} Raman band after the cell polarization returns to OCV from -1V. When the bias is reversed from -1V to +1V, the kinetics of such a transformation would simply be too fast for experiments to report the Mn$_3$O$_4$ intermediate growth. This hypothesis is supported by a weak decrease in Mn$_3$O$_4$ signal at the end of the cathodic polarization (Figure 4c).

Finally, an additional observation associated with MnO$_x$ segregation on the electrode surface is that the segregation was only observed on LSM electrodes with BaO. A number of LSM thin film electrodes without BaO deposition were subjected to various treatments, including higher temperatures (700 °C) and stronger polarizations (-2.5V) than those applied to the BaO modified electrodes.[48] Despite these more extreme conditions, an increase in the amount of Mn$_3$O$_4$ was not observed with Raman spectroscopy during any of the polarizations[48]. The fact that changes in Mn$_3$O$_4$ were not observed on the pure LSM electrodes suggests that the Ba$_3$Mn$_2$O$_8$ secondary phase is a dominant source for Mn$_3$O$_4$ formation, although Ba diffusion into the LSM electrode (Figure 2) can have influenced Mn segregation. Regarding the amount of Ba, which can be accommodated in LSM, experiments have shown that lanthanum manganates are stable with up to 40% substitution of Ba on the La site.[49] However, a recent study of lanthanum manganite thin films has shown that the maximum substitution level is strongly dependent on temperature and oxygen partial pressure.[50]

The Ba$_3$Mn$_2$O$_8$ secondary phase on LSM electrodes infiltrated with BaO was most likely formed via a reaction with excess MnO$_x$ in the electrode. The behavior of this secondary

phase and of MnO$_x$ phases during polarization has been discussed above, and in Eq. (1)-(3) the proposed cathode reactions are summarized.

$$14\ e^- + 3\ Ba_3Mn_2O_8 \rightarrow 2Mn_3O_4 + 9\ BaO + 7\ O^{2-} \tag{1}$$

$$LSM_{ox} + 2\ e^- \rightarrow LSM_{red} + Mn_3O_4 + MnO + O^{2-} \tag{2}$$

$$Mn_3O_4 + 2\ e^- \rightarrow 3\ MnO + O^{2-} \tag{3}$$

So far it has been suggested that Ba$_3$Mn$_2$O$_8$ is responsible for the reduced polarization resistance observed on the BaO infiltrated LSM electrodes at OCV conditions. Furthermore the removal of Ba$_3$Mn$_2$O$_8$ and the associated changes in the electrode surface composition during cathodic polarization has been thoroughly discussed. Still unresolved is how these compositional changes during polarization influence electrode performance. A common issue in LSM electrodes and other perovskite based electrodes is passivation of the electrode surface due to segregation of Sr and impurities to the surface.[28] We suggest that reduction of Ba$_3$Mn$_2$O$_8$ releasing Mn$_3$O$_4$ and MnO onto the electrode surface will increase the electrochemical activity. This suggestion is based on literature reportings showing decreased polarization resistance in oxygen atmospheres on LSM electrodes infiltrated with MnO$_x$ [51, 52] or Pt-YSZ electrodes modified with Mn-species[53]. Since very limited reports are made on the electrocatalytic properties of MnO$_x$, further experiments are needed to test the hypothesis that the release of Mn$_3$O$_4$ and/or MnO one the electrode surface increases the electrochemical activity of the BaO infiltrated electrodes during operation.

4. Conclusion

The experiments on BaO modified LSM electrodes described in this work were conducted to explore how the addition of BaO affects the LSM electrodes' electrocatalytic properties, particularly as an O$_2$ reduction catalyst. The enhanced electrocatalytic properties caused by

the BaO modification is, based on this work, at OCV conditions ascribed to formation of a secondary $Ba_3Mn_2O_8$ phase. During cathodic polarization a significant redistribution of elements in the electrode surface takes place, as the $Ba_3Mn_2O_8$ phase decomposes and MnO_x species accumulates in the electrode surface. The redistributions are reversible with polarization, thus the electrode returns to the original state when polarized in the anodic direction or returned to OCV. These reversible changes illustrate that element or material specific techniques must be applied *in operando*, to envisage the active state during operation of an infiltrated LSM electrode, or any other solid electrode prepared infiltration. Knowing the exact electrode composition during operation is a crucial prerequisite for understanding why the widespread use of infiltration in electrode preparation improves the electrocatalytic properties of solid electrodes. Another consequence of results reported herein is recognition that compounds such as $Ba_3Mn_2O_8$ that include a highly oxidized transition metal can serve as a "storage" compound for the transition metal until polarization is applied and the transition metal having high electrocatalytic activity is "released" or redistributed onto the electrode surface. Further research is however needed in order to explorer this intriguing concept in more detail.

5. Experimental Section

5.1 Sample architecture and materials selection

In commercial applications of infiltrated LSM electrodes, the electrode is typically a porous composite electrode with the primarily electron-conducting LSM perovskite entangled with an oxygen-ion conducting electrolyte.[54, 55] Common electrolyte materials are YSZ for operating temperatures > 600 °C and CGO for operating temperatures < 600 °C.[56] However, in this work the majority of the *in operando* experiments were performed using a thin film model electrode in order to ensure uniform polarization of the electrode. To assure consistency between thin film model electrodes and conventional porous composite electrodes,

both electrode types were fabricated and Raman spectra were recorded from each electrode type. Sketches of the electrochemical cells with thin film and porous electrodes respectively are shown in Figure 7.
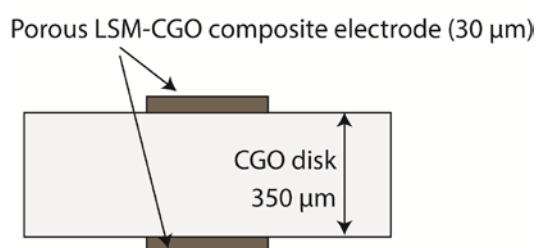
a)
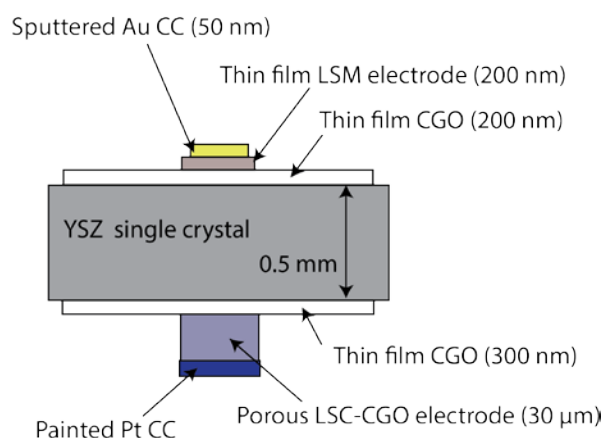
b)

Figure 7. Sketch of the electrochemical cells applied in this work a) the thin film model cell and b) the "conventional cell" with porous LSM-CGO electrode. CC denotes the current collector.

Experiments described below used LSM as the electron conducting phase due to this material's structural stability and its widespread usage in solid oxide electrolysis/fuel cells[54, 57, 58] and electrochemical cells intended to remediate NO$_x$ pollutants from diesel exhaust

streams.[20] Gadolinium-doped ceria (CGO) served as the electrolyte phase in the conventional cells with porous electrodes due to CGO's high oxygen ion conductivity at comparatively low temperatures (<600 °C).[56] Furthermore, a CGO thin film layer was applied adjacent to the LSM thin film electrode in the thin film model cell to mimic the materials composition of the conventional cells. For the thin film model cell, a YSZ single crystal served as both the electrolyte and substrate for the CGO and LSM thin films due to the lack of commercially available CGO single crystals. In accordance with these considerations, LSM15 (($La_{0.85}Sr_{0.15})_{0.9}MnO_{3\pm\delta}$), CGO10 ($Ce_{0.90}Gd_{0.10}O_{1.95}$) and for the thin film samples additionally YSZ (($Y_2O_3)_{9.5}(ZrO_2)_{90.5}$), were used in the experiments described below.

5.2 Fabrication of electrochemical thin film model cell

The thin film model cell was designed to mimic conventional cells with a composite electrode consisting of an oxygen conducting CGO phase and an electronic conducting LSM phase. A previous study on this type of model cell has been reported elsewhere with further details on the cell preparation[48]. The YSZ single crystals (CrysTeC GmbH, Germany) that served as electrolyte and substrate for the thin films had a (100) exposed face, were single side polished and measured 2.54 cm in diameter. The LSM thin film electrode and thin films of CGO were deposited on the YSZ using pulsed laser deposition (PLD) with a KrF excimer laser. During the depositions, the fluence was 2 Jcm^{-2} with a laser frequency of 10 Hz and the distance between the substrate and target was 7.5 cm. The CGO thin films (200-300 nm) were deposited at a substrate temperature of 700 °C and oxygen partial pressure of 5 x 10^{-4} mbar on both the polished and the rough side of the YSZ single crystal. The LSM thin film electrode (≈200 nm) was deposited on top of the CGO layer on the polished side of the YSZ single crystal and a shadow mask maintained LSM thin film electrode dimensions of 0.5 cm x 1 cm. The LSM deposition was conducted with a substrate temperature of 600 °C and with oxygen

partial pressure at 7 x 10^{-4} mbar. The oxygen partial pressure was increased to 0.02 mbar immediately after the deposition and during cool-down to avoid oxygen deficiencies from developing in the LSM electrode. An LSC-CGO (50 wt% $(La_{0.6}Sr_{0.4})_{0.99}CoO_3$-50 wt% $Ce_{0.9}Gd_{0.1}O_{1.95}$) porous electrode (30 µm) was screen-printed as a "counter-electrode" to the thin film LSM electrode and was deposited on top of the CGO thin film on the rough side of the YSZ single crystal. Following the application of the LSC-CGO electrode, the entire electrochemical cell was heated to 930 °C for 24 h. A Pt current collector was painted on the LSC-CGO electrode and sintered at 900 °C for 2 h. Finally, Au was sputtered onto the thin film electrode and the cell was heat-treated at 700 °C for 120 h allowing the Au to sinter, with the intention of forming a continuous Au network for current collection. As subsequent imaging revealed the formation of separate μm-sized Au particles rather than an Au network, adequate current collection was obtained by applying an Au mesh in the final test-set-up. The complete architecture of the thin film model cell is shown in Figure 7 a) and a SEM image of the LSM thin film electrode and the adjacent layers is found in SI-7.

5.3 Preparation of "conventional" electrochemical cell with porous LSM-CGO electrodes

Electrochemical cells with porous LSM-CGO composite electrodes were prepared as follows: a CGO10 (Rhodia) electrolyte with 1% Fe added as a sintering aid was tape-casted, stamped out in disks and sintered at a maximum temperature of 1250 °C for 4 h. After sintering, the electrolyte disks were dense, 350 µm thick and had a diameter of 23 mm. A circular 10 mm diameter 50 wt% LSM15 – 50 wt% CGO10 composite electrode was screen-printed onto each side of the CGO electrolyte disks and sintered with the maximum temperature of 1050 °C for 2 h, resulting in ≈30 µm thick porous electrodes. A sketch of the cell with porous LSM-CGO electrodes is shown in Figure 7 b)

5.4 Addition of BaO

BaO was added to both a dense, thin film LSM electrode and a porous LSM-CGO electrode. Due to reaction with CO_2 in the atmosphere and reaction with the electrode components, the majority of the Ba added was present as $BaCO_3$ or as Ba-Mn-O compounds (*vide supra*) throughout the *in operando* experiments; however for brevity, these samples are referred to as BaO-infiltrated samples. Due to differences in sample architecture between the thin film LSM electrode and a porous LSM-CGO electrode, slightly different procedures were used for the BaO addition. The porous LSM-CGO electrodes were infiltrated by adding a droplet of 0.32 M $Ba(NO_3)_2$ (aq) onto the electrode surface and the solution was allowed to soak into the porous structure. Excess solution was removed from the surface and the infiltrated cells were heat-treated at 700 °C for 1 h to decompose the $Ba(NO_3)_2$ into BaO. This procedure was repeated 7 times to obtain a uniform coverage of ≈50 nm BaO particles throughout the electrodes. A similar procedure was employed for deposition of $Ba(NO_3)_2$ onto the LSM thin film electrodes, where an aqueous 0.032 M $Ba(NO_3)_2$ solution containing 10 wt% P123 dispersant (BASF) was used. Excess solution on the thin film electrodes was not wiped off of the surface prior to the heat-treatment at 700 °C and the $Ba(NO_3)_2$ deposition step was only performed once. This procedure resulted in large agglomerations of BaO on some areas of the electrode (Figure 8a), while in other areas nanosized BaO particles were well dispersed on the electrode surface as intended. It is emphasized that the *in operando* Raman spectroscopy reported in this paper was conducted on the electrode area with well-dispersed BaO. Top-view SEM images of an electrode area with BaO present as nanoparticles is shown in Figure 8b and a bare LSM thin film electrode for comparison is shown in Figure 8c. The BaO particles on the surface caused the BaO treated electrode to appear more "roughened" (Figure 8b) compared to the non-infiltrated surface (Figure 8c).
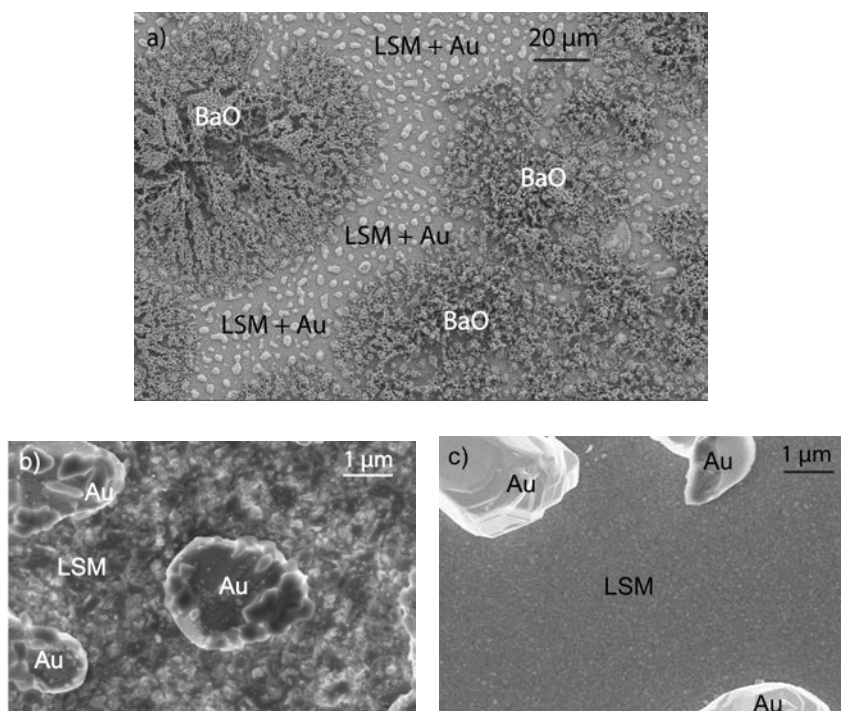
Figure 8. Top-view SEM images of the LSM thin film electrodes a, b) with BaO deposition and c) without BaO deposition.

5.5 SEM

Electrode surfaces and cross-sections of broken cells were investigated with scanning electron microscopy (SEM) on a Zeiss Supra 35 microscope. The microstructure of the electrode surfaces was investigated using the InLens detector with a 5 kV acceleration voltage and without any pre-treatment of the electrode. The thickness of the thin film layers of broken cross-sections was determined using the backscattered electron detector with a 10 kV acceleration voltage and the cross sections were carbon coated to avoid charging of the sample.

5.6 TOF-SIMS

Analysis of the elemental distribution through LSM thin film electrodes without and with BaO deposition was performed with Time-of-Flight Secondary Ion Mass Spectrometry (TOF-SIMS) using a TOF-SIMS IV (ION-TOF GmbH, Münster, Germany). The 25 ns pulses of 25

keV Bi$^+$ (primary ions) were used at a repetition rate of 10 kHz, yielding a target current of

0.7 pA. Depth profiling was performed with approximately 2 nm depth resolution on a

200×200 µm^2 surface analysis area centered in a 300×300 µm^2 sputter area. The 30 nA of 3

keV Xe$^+$ was used as sputter ions (10 s sputtering, 1 s pause and then analysis using one scan

and 256×256 pixels). For all analyses electron bombardment (20 eV) was used to minimize

charge built-up at the surface. Desorbed secondary ions were accelerated to 2 keV, mass

analyzed in the flight tube, and post-accelerated to 10 keV before detection.

5.7 XPS

The surface stoichiometry of four LSM thin film electrodes without BaO deposition were

analysed with X-ray photoelectron spectroscopy (XPS) performed on a K-alpha (Thermo

Electron Limited, Winsford, UK) using a monochromated Al-K-α X-ray source and a take-off

angle of 90° from the surface plane. Atomic concentrations were determined from surface

spectra (0–1350 eV, 100 eV detector pass energy) and were calculated by determining the

relevant integral peak intensities using a Shirley type background. Each sample surface was

analyzed at three different surface locations and the average value for all four samples is

reported in the results section.

5.8 Raman Spectroscopy

In operando Raman spectra were acquired using a Renishaw InVia spectrometer with a 488

nm Ar-ion laser and Pelletier cooled charge-coupled device (CCD) detector. The cells were

mounted in an assembly developed originally to perform *in operando* studies of solid oxide

cells and has been described in more detail elsewhere.[59, 60] Cells were fixed on the end of an

YSZ tube with YS2B glass paste (IRD Fuel Cell AS) and gold wires were attached to the

current collectors for electrochemical measurements. This assembly was then enclosed with a

quartz tube (Quark Glass) and placed inside a tube furnace. Optical access to the thin film

electrode was maintained for Raman spectroscopic measurements and visual inspection. In this system, the cell was tested in a two-atmosphere environment at elevated temperatures. The laser power out of the spectrometer was 18 mW and this laser power was selected to give the best possible signal-to-noise ratio without causing damage to the samples. It is noted that due to scattering losses from the optics the power was slightly lower at the electrode surface.During the *in operando* experiments, Raman spectra with 20 s exposure times were continuously collected to record changes in the surface species under applied potential.

5.9 Electrochemical characterization

A potential was applied on the electrochemical cell using a Gamry Reference 600 potentiostat to record chronoamperometry curves. The applied potential difference was either -1 V or +1 V and the potential difference was predominantly across the thin film electrode, as the resistance of the porous LSC-CGO electrode was <1% of the resistance of the LSM thin film electrode. This was experimentally confirmed by using electrochemical impedance spectroscopy to determine the polarization resistance on symmetric cells with two LSC-CGO electrodes and on cells with one LSC-CGO electrode and one LSM thins film electrode, respectively.

5.10 Overall experimental sequence

In operando Raman spectra were acquired from a BaO-modified LSM thin film cell during 15 individual polarization experiments that comprised a single overall experimental sequence. At the beginning of the sequence the cell was exposed to a constant gas flow of 10% O_2 in Ar and heated to 500 °C. When at 500 °C, the individual experiments were conducted at -1 V or +1 V. The temperature was then reduced to 300 °C and experiments were repeated. During the experimental sequence, the cell was constantly subjected to a gas flow containing 10% O_2.

5.11 XRD

For phase-determination on the screen-printed electrodes and synthesized $Ba_3Mn_2O_8$ (see next section), XRD measurements were performed at room temperature with a Bruker D8 XRay Diffractometer (Bruker-Siemens, Germany) using Cu Kα radiation with an acceleration voltage of 40 kV and a filament current of 40 mA. The recorded spectra were background corrected using the EVA software (Bruker), and the crystallographic database available in the EVA software was used to identify the present phases.

5.12 Reference materials

During the course of the *in operando* Raman experiments, vibrational bands appeared that could not be assigned to the original materials. Consequently, several new 'candidate' materials were chosen for analysis and served as spectroscopic reference data. Many of these materials were available from traditional sources and/or spectra were already available from the literature. These materials included SrO[61], La_2O_3[62], Mn_2O_3 [32, 33, 36], Mn_3O_4 [32, 33, 36], MnO_2[32, 33, 36], MnO[32], BaO[63, 64], and $BaMnO_3$[65]. One material that was relatively poorly characterized by Raman spectroscopy was $Ba_3Mn_2O_8$, which was synthesized in our own laboratory and characterized by XRD and Raman spectroscopy; see SI-2 for further information about synthesis and characterization of this material.

Supporting Information

Supporting Information is available from the Wiley Online Library or from the author.

Acknowledgements

References

[1] J. Larminie, A. Dicks, *Fuel Cell Systems Explained, 2nd edition*, John Wiley & Sons Ltd, England **2003**.

[2] M. A. Laguna-Bercero*, J. Power Sources.* **2012***, 203*, 4.

[3] K. K. Hansen*, Appl. Catal. , B.* **2010***, 100*, 427.

[4] S. P. Jiang*, Mater. Sci. Eng. A.* **2006***, 418*, 199.

[5] D. Ding, X. Li, S. Y. Lai, K. Gerdes, M. Liu, *Energy Environ. Sci.* **2014***, 7*, 552.

[6] A. J. Samson, M. Sogaard, P. Hjalmarsson, J. Hjelm, N. Bonanos, S. P. V. Foghmoes, T. Ramos, *Fuel Cells.* **2013***, 13*, 511.

[7] N. Ai, S. P. Jiang, Z. Lue, K. Chen, W. Su, *J. Electrochem. Soc.* **2010***, 157*, B1033.

[8] M. Sase, K. Yashiro, K. Sato, J. Mizusaki, T. Kawada, N. Sakai, K. Yamaji, T. Horita, H. Yokokawa, *Solid State Ionics.* **2008***, 178*, 1843.

[9] J. Hayd, H. Yokokawa, E. Ivers-Tiffee, *J. Electrochem. Soc.* **2013***, 160*, F351.

[10] E. Mutoro, E. J. Crumlin, M. D. Biegalski, H. M. Christen, Y. Shao-Horn, *Energy Environ. Sci.* **2011***, 4*.

[11] M. Backhaus-Ricoult, K. Adib, T. St.Clair, B. Luerssen, L. Gregoratti, A. Barinov, *Solid State Ionics.* **2008***, 179*, 891.

[12] E. Siebert, A. Boréave, F. Gaillard, T. Pagnier, *Solid State Ionics.* **2013***, 247–248*, 30.

[13] C. W. Sun, R. Hui, J. Roller, *J. Solid State Electrochem.* **2010***, 14*, 1125.

[14] Y. Huang, J. M. Vohs, R. J. Gorte, *Electrochem. Solid-State Lett.* **2006**, *9*, A237.

[15] T. Z. Sholklapper, C. Lu, C. P. Jacobson, S. J. Visco, L. C. De Jonghe, *Electrochem. Solid-State Lett.* **2006**, *9*, A376.

[16] J. M. Vohs, R. J. Gorte, *Adv Mater.* **2009**, *21*, 943.

[17] V. A. C. Haanappel, D. Rutenbeck, A. Mai, S. Uhlenbruck, D. Sebold, H. Wesemeyer, B. Rowekamp, C. Tropartz, F. Tietz, *J. Power Sources.* **2004**, *130*, 119.

[18] C. C. Kan, E. D. Wachsman, *J. Electrochem. Soc.* **2009**, *156*, B695.

[19] F. Bidrawn, G. Kim, N. Aramrueang, J. M. Vohs, R. J. Gorte, *J. Power Sources.* **2010**, *195*, 720.

[20] R. M. L. Werchmeister, K. K. Hansen, M. Mogensen, *Mater. Res. Bull.* **2010**, *45*, 1554.

[21] M. L. Traulsen, K. B. Andersen, K. K. Hansen, *J. Mater. Chem.* **2012**, *22*, 11792.

[22] J. Shao, K. K. Hansen, *J. Mater. Chem. A.* **2013**, *1*, 7137.

[23] D. Ippolito, K. B. Andersen, K. K. Hansen, *J. Electrochem. Soc.* **2012**, *159*, P57.

[24] T. Hong, F. Chen, C. Xia, *Electrochem. Commun.* **2015**, *51*, 93.

[25] J. Shao, K. K. Hansen, *J. Electrochem. Soc.* **2013**, *160*, H494.

[26] K. Norrman, K. V. Hansen, T. Jacobsen, *RSC advances.* **2015**, *5*, 87679.

[27] W. Wang, S. P. Jiang, *Solid State Ionics.* **2006**, *177*, 1361.

[28] J. Druce, H. Tellez, J. Hyodo, *MRS Bull.* **2014**, *39*, 810.

[29] M. T. Weller, S. J. Skinner, *Acta Crystallogr. , Sect. C: Cryst. Struct. Commun.* **1999**, *55*, 154.

[30] A. Feinberg, C. H. Perry, *J. Phys. Chem. Solids.* **1981**, *42*, 513.

[31] E. F. Lopez, V. S. Escribano, M. Panizza, M. M. Carnasciali, G. Busca, *J. Mater. Chem.* **2001**, *11*, 1891.

[32] M. C. Bernard, A. H. Goff, B. V. Thi, S. C. Detorresi, *J. Electrochem. Soc.* **1993**, *140*, 3065.

[33] F. Buciuman, F. Patcas, R. Craciun, D. Zahn, *Phys. Chem. Chem. Phys.* **1999**, *1*, 185.

[34] E. Widjaja, J. T. Sampanthar, *Anal. Chim. Acta.* **2007**, *585*, 241.

[35] T. Gao, H. Fjellvag, P. Norby, *Anal. Chim. Acta.* **2009**, *648*, 235.

[36] W. Hong, M. Ueda, S. Iwamoto, S. Hosokawa, K. Wada, M. Inoue, *Catal. Lett.* **2012**, *142*, 32.

[37] N. Mironova-Ulmane, A. Kuzmin, M. Grube, *J. Alloys Compounds.* **2009**, *480*, 97.

[38] W. Kaabar, S. Bott, R. Devonshire, *Spectrochim. Acta Mol. Biomol. Spectrosc.* **2011**, *78*, 136.

[39] B. Banov, A. Momchilov, M. Massot, C. M. Julien, *Mater. Sci. Eng. , B.* **2003**, *100*, 87.

[40] D. Uy, K. Wiegand, A. O'Neill, M. Dearth, W. Weber, *J. Phys. Chem. B.* **2002**, *106*, 387.

[41] C. B. Azzoni, M. C. Mozzati, P. Galinetto, A. Paleari, V. Massarotti, D. Capsoni, M. Bini, *Solid State Commun.* **1999**, *112*, 375.

[42] J. Roos, C. Eames, S. M. Wood, A. Whiteside, M. S. Islam, *Phys. Chem. Chem. Phys.* **2015***, 17*, 22259.

[43] A. Hammouche, E. Siebert, A. Hammou, M. Kleitz, A. Caneiro, *J. Electrochem. Soc.* **1991***, 138*, 1212.

[44] J. Mizusaki, N. Mori, H. Takai, Y. Yonemura, H. Minamiue, H. Tagawa, M. Dokiya, H. Inaba, K. Naraya, T. Sasamoto, T. Hashimoto, *Solid State Ionics.* **2000***, 129*, 163.

[45] B. Zachau-Christiansen, T. Jacobsen, S. Skaarup, *SOFC V.* **1997***, 97-40*, 795.

[46] M. K. Mahapatra, S. Bhowmick, N. Li, P. Singh, *J. Eur. Ceram. Soc.* **2012***, 32*, 2341.

[47] E. C. Samulon , *Dissertation thesis.* **2011***, Stanford University*.

[48] M. D. McIntyre, M. L. Traulsen, K. Norrman, S. Sanna, R. A. Walker, *ECS Trans.* **2015***, 66*, 47.

[49] A. Chakraborty, P. Devi, H. Maiti, *J. Mater. Res.* **1995***, 10*, 918.

[50] W. Lee, J. W. Han, Y. Chen, Z. Cai, B. Yildiz, *J. Am. Chem. Soc.* **2013***, 135*, 7909.

[51] M. L. Traulsen, K. Kammer Hansen, *J. Electrochem. Soc.* **2011***, 158*.

[52] A. Babaei, L. Zhang, E. Liu, S. P. Jiang, *J. Alloys Compounds.* **2011***, 509*, 4781.

[53] A. J. McEvoy*, Solid State Ionics.* **2000***, 135*, 331.

[54] S. P. Jiang*, J. Mater. Sci.* **2008***, 43*, 6799.

[55] Y. Yoshinobu, Y. Tsuda, H. Ueda, Y. Nakanishi, J. Gong, *SAE Int.J.Fuels Lubr.* **2010***, 3*, 50.

WILEY-VCH

[56] B. Dalslet, P. Blennow, P. V. Hendriksen, N. Bonanos, D. Lybye, M. Mogensen, *J. of Solid State Electrochem.* **2006***, 10*, 547.

[57] S. Adler*, Chem. Rev.* **2004***, 104*, 4791.

[58] A. Hauch, S. D. Ebbesen, S. H. Jensen, M. Mogensen, *J. Mater. Chem.* **2008***, 18*, 2331.

[59] M. B. Pomfret, J. C. Owrutsky, R. A. Walker, *J. Phys. Chem. B.* **2006***, 110*, 17305.

[60] M. B. Pomfret, J. C. Owrutsky, R. A. Walker, *Annu. Rev. Anal. Chem.* **2010***, 3*, 151.

[61] K. H. Rieder, B. A. Weinstein, M. Cardona, H. Bilz, *Phys. Rev. B.* **1973***, 8*, 4780.

[62] A. Orera, G. Larraz, M. L. Sanjuan, *J. Eur. Ceram. Soc.* **2013***, 33*, 2103.

[63] G. Mestl, M. P. Rosynek, J. H. Lunsford, *J. Phys. Chem. B.* **1998***, 102*, 154.

[64] D. de Waal, K. Range, M. Konigstein, W. Kiefer, *J. Raman Spectrosc.* **1998***, 29*, 109.

[65] C. Roy, R. C. Budhani, *J. Appl. Phys.* **1999***, 85*, 3124.

The table of contents entry:

In operando **Raman spectroscopy reveals unexpected changes in the surface composition** of BaO infiltrated LSM electrodes during operation. A secondary $Ba_3Mn_2O_8$ phase forms during fabrication and reversibly decomposes during cathodic polarization leading to MnO_x accumulation at the electrode surface. These changes illustrate that infiltrated electrode performance may arise from unanticipated changes in composition that can only be monitored *in operando*.

M. L. Traulsen*, M. D. McIntyre, K. Norrman, S. Sanna, M. B. Mogensen and R. A. Walker

Reversible Decomposition of Secondary Phases in BaO Infiltrated LSM Electrodes – Polarization Effects

ToC figure